Downloaded from orbit.dtu.dk on: Jun 03, 2024

DTU Library

Nanoscale Disorder and Deintercalation Evolution in K-Doped MoS_2 Analysed Via In Situ TEM

Shao, Shouqi; Tainton, Gareth R.M.; Kuang, W. J.; Clark, Nick; Gorbachev, Roman; Eggeman, Alexander; Grigorieva, Irina V.; Kelly, Daniel J.; Haigh, Sarah J.

Published in:
Advanced Functional Materials

Link to article, DOI:
10.1002/adfm.202214390

Publication date:
2023

Document Version
Publisher's PDF, also known as Version of record

Link back to DTU Orbit

Citation (APA):
Shao, S., Tainton, G. R. M., Kuang, W. J., Clark, N., Gorbachev, R., Eggeman, A., Grigorieva, I. V., Kelly, D. J., & Haigh, S. J. (2023). Nanoscale Disorder and Deintercalation Evolution in K-Doped MoS_2 Analysed Via In Situ TEM. *Advanced Functional Materials*, *33*(30), Article 2214390. https://doi.org/10.1002/adfm.202214390

General rights
Copyright and moral rights for the publications made accessible in the public portal are retained by the authors and/or other copyright owners and it is a condition of accessing publications that users recognise and abide by the legal requirements associated with these rights.

- Users may download and print one copy of any publication from the public portal for the purpose of private study or research.
- You may not further distribute the material or use it for any profit-making activity or commercial gain
- You may freely distribute the URL identifying the publication in the public portal

If you believe that this document breaches copyright please contact us providing details, and we will remove access to the work immediately and investigate your claim.

ADVANCED FUNCTIONAL MATERIALS
www.afm-journal.de

Check for updates

Nanoscale Disorder and Deintercalation Evolution in K-Doped MoS_2 Analysed Via In Situ TEM

Shouqi Shao, Gareth R.M. Tainton, W. J. Kuang, Nick Clark, Roman Gorbachev, Alexander Eggeman, Irina V. Grigorieva, Daniel J. Kelly,* and Sarah J. Haigh**

Intercalation and deintercalation processes in van der Waals crystals underpin their use in nanoelectronics, energy storage, and catalysis but there remains significant uncertainty regarding these materials' structural and chemical heterogeneity at the nanoscale. Deintercalation in particular often controls the robustness and cyclability of the involved processes. Here, a detailed analysis of potassium ordering and compositional variations in as-synthesised K intercalated MoS_2 as well an analysis of deintercalation induced changes in the structure and K/Mo elemental composition is presented. By combining 4D scanning transmission electron microscopy (4DSTEM), in situ atomic resolution STEM imaging, selected area electron diffraction (SAED) and energy dispersive X-ray spectroscopy (EDS) the formation of previously unknown intermediate superstructures during deintercalation is revealed. The results provide evidence supporting a new deintercalation mechanism that favors formation of local regions with thermodynamically stable ordering rather than isotropic release of K. Systematic time-temperature measurements demonstrate the deintercalation behavior to follow first-order kinetics, allowing compositional and superstructural changes to be predicted. It is expected that the in situ correlative STEM-EDS/SAED methodology developed in this work has the potential to determine optimal synthesis, processing and working conditions for a variety of intercalated or pillared materials.

1. Introduction

Intercalation of dopant atoms and ions into the layers of van der Waals crystals such as graphite, transition metal dichalcogenides (TMDCs), and MXenes allows tuning the material's chemical, electronic and optical properties.[1–9] Among the family of intercalated 2D materials and possible dopant atom species, alkali metal-intercalated MoS_2 has attracted considerable interest in catalysis, nanoelectronics, and optoelectronics as intercalation allows tuning of the band structure.[9–12] However, the materials' in service lifetime for these applications is often limited unless the spontaneous deintercalation process, where intercalant is released from the host crystal lattice, is effectively controlled. These materials also find applications as electrocatalysts, supercapacitors and batteries, since the weak van der Waals interlayer bonding enables these materials' ability to withstand numerous intercalation and deintercalation cycles.[13,14] Many studies consider the intercalation behavior of MoS_2 as a model transition metal dichalcogenide, but intercalated crystals are complex at the nanoscale and the evolution of structure and chemistry during deintercalation has never been quantitatively studied at the nanometer scale.

The mechanism of alkali metals intercalation in MoS_2 is underpinned by its electronic band structure, density of states and the availability of intercalation sites.[15] 2H-MoS_2 has a layered structure with Mo atoms in trigonal prismatic sites; its d_z^2 band is filled up with two electrons, so that the material is a semiconductor. Due to their low electrochemical potential, when alkali metal atoms (Li, Na, K) intercalate they donate an electron from their valence *s* orbital to the electronic levels above the band gap, leading to the metallic behavior of the intercalated

S. Shao, G. R.M. Tainton, N. Clark, A. Eggeman, D. J. Kelly, S. J. Haigh
Department of Materials
University of Manchester
Oxford Road, Manchester M13 9PL, UK
E-mail: dankel@dtu.dk; sarah.haigh@manchester.ac.uk

The ORCID identification number(s) for the author(s) of this article can be found under https://doi.org/10.1002/adfm.202214390.

© 2023 The Authors. Advanced Functional Materials published by Wiley-VCH GmbH. This is an open access article under the terms of the Creative Commons Attribution License, which permits use, distribution and reproduction in any medium, provided the original work is properly cited.

[+]Present address: National Innovation Institute of Defense Technology, AMS, Beijing 100071, China

S. Shao, G. R.M. Tainton, N. Clark, R. Gorbachev, I. V. Grigorieva, D. J. Kelly, S. J. Haigh
National Graphene Institute
University of Manchester
Oxford Road, Manchester M13 9PL, UK
E-mail: irina.v.grigorieva@manchester.ac.uk

W. J. Kuang,[+] R. Gorbachev, I. V. Grigorieva
Department of Physics and Astronomy
University of Manchester
Oxford Road, Manchester M13 9PL, UK

D. J. Kelly
DTU Nanolab
Technical University of Denmark
Kgs. Lyngby DK-2800, Denmark

DOI: 10.1002/adfm.202214390

 © 2023 The Authors. Advanced Functional Materials published by Wiley-VCH GmbH

16163028, 0, Downloaded from https://onlinelibrary.wiley.com/doi/10.1002/adfm.202214390 by Danish Technical Knowledge, Wiley Online Library on [14/06/2023]. See the Terms and Conditions (https://onlinelibrary.wiley.com/terms-and-conditions) on Wiley Online Library for rules of use; OA articles are governed by the applicable Creative Commons License

compound. Furthermore, at higher intercalant concentrations, the electron transfer to Mo *d* band results in a structural transition from trigonal prismatic (2H) to octahedral (1T) coordination, which can be understood from comparison of the *d*-band density of states for 2H- and 1T-MoS_2: the occupied bands for 1T are significantly lower in energy. The 2H to 1T transition is also accompanied by an increase in Mo—S bond ionicity, so that coulombic repulsion between partially charged ligands favors the octahedral form.[15] Clustering of transition metal atoms also drives further structural phase transitions to the rarer metallic 1T′/1T″ or the semiconducting 1T‴ phase[3,17,18] (Figure S2, Supporting Information). See also our previous work[11,16] for a further discussion of the intercalation process.

Intercalated TMDC materials are desirable for nanoelectronic applications having a reduced contact resistance[7] and offering new superconducting phases.[12,16] The metallic 1T phase of MoS_2 is also appealing for catalytic applications, for example, enhancing the efficiency of MoS_2 for the hydrogen evolution reaction compared to the more thermodynamically favored 2H phase.[19] The electronically and catalytically desirable 1T phase has been found to persist even after deintercalation, although optimal deintercalation conditions that prevent the transformation back to 2H and loss of preferred electronic structure whilst removing deleterious effects from remnant alkali elements, have yet to be experimentally verified. Deintercalation occurs spontaneously in these materials on exposure to heat,[20] air,[11,16] and moisture[21] so must be understood for the unique properties of these materials to be effectively exploited. It is also necessary to understand the deintercalation behavior of TMDCs due to the importance of intercalation/deintercalation cyclability when designing materials for next generation batteries and supercapacitor systems.[22–24]

Transmission electron microscopy (TEM) is one of the few techniques able to provide nanoscale structural and chemical information to aid in understanding intercalation and deintercalation processes.[11,24–28] In situ electrical biasing in the TEM has shown that Li intercalation in MoS_2 induces a 2H to 1T phase transition and the formation of ordered Li ion superstructures, although deintercalation was not explored as the material transformed to amorphous LiS_2 at long lithiation times.[24,25] In situ TEM electrical biasing has also revealed that Na ion intercalated MoS_2 contains significant lattice disorder with locally ordered domains at the 3–5 nm length scale.[26,27] However, K intercalation is less well studied than Na and Li, and deintercalation dynamics are entirely unexplored by TEM. Additionally, most in situ TEM studies have not employed complementary elemental analysis to correlate local structure and composition for intercalated compounds, and no such information is available for the deintercalation process.

Here a nanoscale in situ TEM investigation of deintercalation in K-intercalated MoS_2 is presented to characterize the structural and chemical changes that occur under annealing at different temperatures. Multiple in situ electron microscopy methods (electron diffraction (ED), high-resolution TEM (HR-TEM), STEM) and quantitative energy dispersive X-ray spectroscopy (EDS) spectrum imaging) are combined with 4D scanning transmission electron microscopy. This direct correlation of local crystal structure and composition provides evidence of new K-MoS_2 superstructures and sheds light on the local nanostructure and quantitative compositional evolution occurring during alkali ion deintercalation for TMDCs.

2. Nanoscale Structural and Elemental Characterization of Intercalated MoS_2

To achieve K intercalation we used the well-known liquid-ammonia method.[29] In brief, MoS_2 powder consisting of few-micron size crystalline flakes is immersed in a liquid ammonia solution containing K at -78°C for 24 hours (see SI Figure S3c, Supporting Information for size and thickness distribution). Dissolved K atoms dissociate into solvated cations (K^+) and solvated electrons (e^-) as evident from the deep blue colour of the ammonia solution:[30,31] The color is the result of the emergence of a broad optical absorption line peaked at 0.85 eV and extending into the visible range.[31] The fact that the colour of the solution and its optical properties have been shown to be independent of the solute[31] is evidence of the presence of solvated electrons: the latter are trapped in cavities formed by the polar ammonia molecules and are responsible for the above optical absorption. As K^+ ions intercalate into the interlayer gallery of the layered crystal, solvated electrons are donated to the empty Mo *d*-bands of 2H-MoS_2 to balance the charge[11] while the potassium-ammonia solution gradually loses its colour, indicating a reduction in the amount of available intercalant in solution. Following intercalation, the dried powder was stored under argon before transferring a thin layer of intercalated crystals onto TEM heating E-chips and rapidly loading these into the TEM to minimize exposure to oxygen (see Methods for further details).

To track the materials' deintercalation behaviour it is necessary to understand the structure of the intercalated starting material at the nanoscale. **Figure 1**a shows a representative HAADF STEM image of a typical K intercalated MoS_2 flake, with Figure 1b the corresponding SAED pattern viewed along [0001], acquired from the area of the selected-area aperture indicated by the red circle in Figure 1a. The size and morphology of the intercalated flake is similar to the pristine MoS_2 starting material, being composed of restacked aggregates of individual crystallites, each having lateral sizes of between 100 nm and a few μm, and thicknesses in the range 1–20 nm. STEM-EDS spectrum imaging of the flake in Figure 1a reveals a mean K/Mo ratio, $n = 0.84$, (equivalent to a stoichiometry of $K_{0.84}MoS_2$, or 21.8 at% K) with K present throughout the flake as shown in Figure 1c, although the single crystal region indicated by the red circle has a slightly lower K/Mo ratio of $n = 0.71$ (equivalent to 19.1 at% K). To ensure reliable K/Mo measurements and avoid contribution from K attached to the surrounding carbon support, threshold-based masking, local averaging and the standardless Cliff Lorimer k-factor analysis were performed (see SI section S5 and SI Figure S18, for further details). The corresponding electron diffraction pattern for this flake (Figure 1b) shows superlattice spots with two-fold periodicity in the direction of the $11\bar{2}0$ and $10\bar{1}0$ reciprocal lattice reflections, thus the superlattice spots closest to the directly transmitted beam are $\frac{1}{2}11\bar{2}0$ and $\frac{1}{2}10\bar{1}0$ (corresponding to distances in real space that are double the $11\bar{2}0$ and $10\bar{1}0$ spacing). The

© 2023 The Authors. Advanced Functional Materials published by Wiley-VCH GmbH

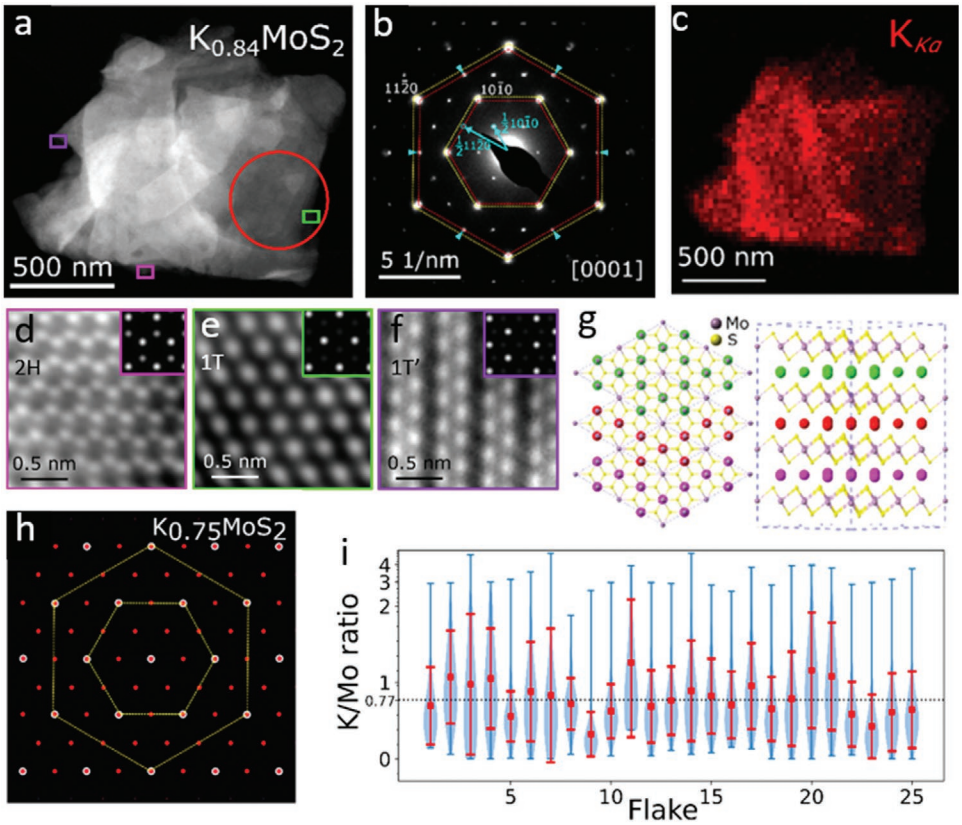

Figure 1. (S)TEM characterization and atomic structure of as-synthesized intercalated K-MoS_2 flakes. a) HAADF STEM image of a K intercalated MoS_2 flake with the average K concentration of 21.9 at% (corresponding to stoichiometry of $K_{0.84}MoS_2$). b) SAED pattern for the area indicated by the red circle in (a). Yellow and red dashed hexagons highlight reflections with different lattice constants corresponding to the pristine MoS_2 and the intercalated phase, respectively. Cyan arrow heads point to the extra superlattice spots seen only in the intercalated phase. c) STEM-EDS K map for the flake in (a).d–f) Experimental HAADF STEM images of regions identified as 2H (trigonal prismatic), 1T (octahedral), and 1T′ (zigzag chains of Mo) phases acquired from the magenta, green and purple rectangles in (a). Simulated HAADF images are inset for reference (see Figure S2, Supporting Information for description of phases). g) Atomic model of $K_{0.75}MoS_2$ used for the diffraction simulation (b), where green, red, and magenta balls indicate K ions arranged in $2a \times 2a$ superlattices in different interlayers. In the plan view model (left) the different atomic layers are off-set for clarity. h) Simulated diffraction pattern of $K_{0.75}MoS_2$ (see panel (g) and Figure S11, Supporting Information for structural model). The MoS_2 lattice reflections are highlighted with white circles while the extra spots from the ordered K are red dots. i) Violin plot of K/Mo ratio in 25 as-synthesized K-intercalated MoS_2 flakes. Red square in each subplot indicates the mean K/Mo ratio for the individual flake, with the standard deviation shown by the red error bars. Blue bars indicate the maximum and minimum measurements, and the shadows illustrate the distribution and local variance in K/Mo ratio for individual flakes.

origin of these superlattice reflections can be assigned either to intercalation-induced zigzag chains of Mo atoms as in the 1T′ structure[32] (see SI Figure S2, Supporting Information), or to ordering of the alkali ions between the layers.[33] To verify the phase of the material we have performed atomic resolution high angle annular dark field (HAADF) STEM imaging of the crystal structure and compared this to image simulations (Figure 1, SI Figures S4, S5, S8). The zigzag chains of the 1T′ phase make it readily distinguishable from the 1T or 2H phases in an atomic resolution image (Figure 1d-f and SI Figure S8, Supporting Information) and from the Fourier transform of a high resolution image (SI Figure S6,S7, Supporting Information). We found the 1T′ structure only in one nanosized region of the flake, spatially remote from the region analysed by electron diffraction (Figure 1a). Other regions showed predominantly 1T phase with limited 2H (Figure 1d,e). Since neither the 2H nor 1T phase produces superlattice reflections, this suggests that the alkaline intercalant is responsible for the superlattice reflections observed in Fig 1b. Potassium is known to prefer to occupy the pseudo-octahedral coordinated interlayer lattice sites in the host MoS_2 lattice and ordered partial filling of these can give rise to superlattice spots.[34] The structure of $K_{0.75}MoS_2$ (n = 0.75) shown in Figure 1g has been predicted previously for alkali metal intercalants in MoS_2,[35] and this reproduces the observed superlattice locations (Figure 1h) as well as only slightly over estimating the locally measured mean elemental analysis (n = 0.71).

However, a closer inspection of the electron diffraction pattern in Figure 1b reveals splitting of the host lattice $11\bar{2}0$ and $10\bar{1}0$ diffraction spots (highlighted by the dashed red and yellow hexagons), which is not present in the simulation. In principle, splitting of diffraction spots can be produced by strain and local bending effects but in this case all spots would be split (including those of the superlattice). Since this feature is only observed for the host lattice spots it must be due to the presence of both the pristine host and expanded intercalated structures (as has been observed previously in $LiMoS_2$[33]). This is confirmed since the outer $11\bar{2}0$ spots correspond to a lattice

© 2023 The Authors. Advanced Functional Materials published by Wiley-VCH GmbH

16163028, 0, Downloaded from https://onlinelibrary.wiley.com/doi/10.1002/adfm.202214390 by Danish Technical Knowledge, Wiley Online Library on [14/06/2023]. See the Terms and Conditions (https://onlinelibrary.wiley.com/terms-and-conditions) on Wiley Online Library for rules of use; OA articles are governed by the applicable Creative Commons License

16163028, 0, Downloaded from https://onlinelibrary.wiley.com/doi/10.1002/adfm.202214390 by Danish Technical Knowledge, Wiley Online Library on [14/06/2023]. See the Terms and Conditions (https://onlinelibrary.wiley.com/terms-and-conditions) on Wiley Online Library for rules of use; OA articles are governed by the applicable Creative Commons License

constant $a = 3.16$ Å (d-spacing = 1.58 Å), which matches pristine 2H or 1T MoS_2 while the inner $11\bar{2}0$ spots are related to twice the superlattice spots, and correspond to a 3% lattice expansion, $a = 3.26$ Å, closer to the structure predicted for $K_{0.75}MoS_2$ by Andersen et al. ($a = 3.36$ Å).[35]

The observed coexistence of different lattice constants and polytypes within an apparently single crystalline region of a flake suggests significant variations in the intercalant content. Earlier work has suggested that in the K_nMoS_2 crystal the 2H phase exists when $n < 0.4$ ($c < 11.8$ at% K), 1T phase for $0.4 < n < 1$ (11.8 at% $< c <$ 25.0 at% K) and the 1T′ phase for $n > 1$ ($c > 25.0$ at%),[11,21] although in the latter case the excess K is reported to cause disintegration of the MoS_2 layers.[11] Mapping the K/Mo ratio of the examined region for the flake of interest (Figure 1d) shows no evidence of a separate region with reduced K content, although the K/Mo ratio in the flake varies at the nanoscale in the range $n < 0.2$ to $n > 1.4$ with a mean of n = 0.68 and a standard deviation of 0.33. Given the correlation of composition and phase proposed by Andersen et al[11] this suggests that the 2H and 1T phases are mixed at the nanoscale, consistent with our atomic resolution imaging results.

STEM-EDS analysis of the pixel-by-pixel composition for twenty-five K-doped MoS_2 flake agglomerates revealed that all contained significant intercalant variations in the as-synthesised condition (Figure 1i). The mean composition was $n = 0.77$ (stoichiometry $K_{0.77}MoS_2$, 20.4 at% K, data shown in SI Figure S1, Supporting Information) with a standard deviation of the flake means ±0.24 (spanning stoichiometry of ~$K_{0.5}MoS_2$ to $KMoS_2$). However, it is notable that even this large standard deviation is smaller than the average variability, ±0.55, seen within each flake (see SI Section S5 for a discussion of efforts made to minimise measurement errors). No systematic differences were observed spatially within the flakes suggesting the morphology is not limiting interlayer K diffusion. Most of the SAED data for intercalated flakes revealed a similar ordering to that shown in Figure 1b. We also saw a flake with an unusually low K content ($n = 0.27$) which revealed a superlattice arrangement not previously reported for this material (SI Figure S9a, Supporting Information). We assign this to a $2a \times \sqrt{3}a$ superstructure arrangement (SI Figure S9b–g), similar to the intermediate intercalation phase previously reported for $Na_{0.25}MoS_2$[27,36] but which has not to our knowledge previously been reported for K intercalation in MoS_2.

From the analysis above it is clear that a severe limitation of comparing TEM selected area electron diffraction data with STEM-EDS elemental mapping is that the spatial resolution of the SAED is >100 nm while STEM-EDS can resolve elemental differences at <1 nm spatial resolution.[37–40] The 4D-STEM[41] approach is superior to SAED in that it allows investigation of the spatial distribution of structural ordering at the nanoscale. A converged electron beam is used to acquire electron diffraction patterns for every image pixel (**Figure 2**) in a single crystal region of a $K_{0.57}MoS_2$ flake (a red square in Figure 2a-c). The average diffraction pattern is shown in Figure 2d revealing superlattice features identical to the $2a \times 2a$ superlattice for $K_{0.55}MoS_2$ shown in SI Figure S10a (Supporting Information), which is assumed to be composed of a regular arrangement of interpenetrating $2a \times 4a$ superlattices. However, applying virtual objective apertures[42,43] at the positions indicated by the red, green and blue disks in Figure 2d reveals that the regions

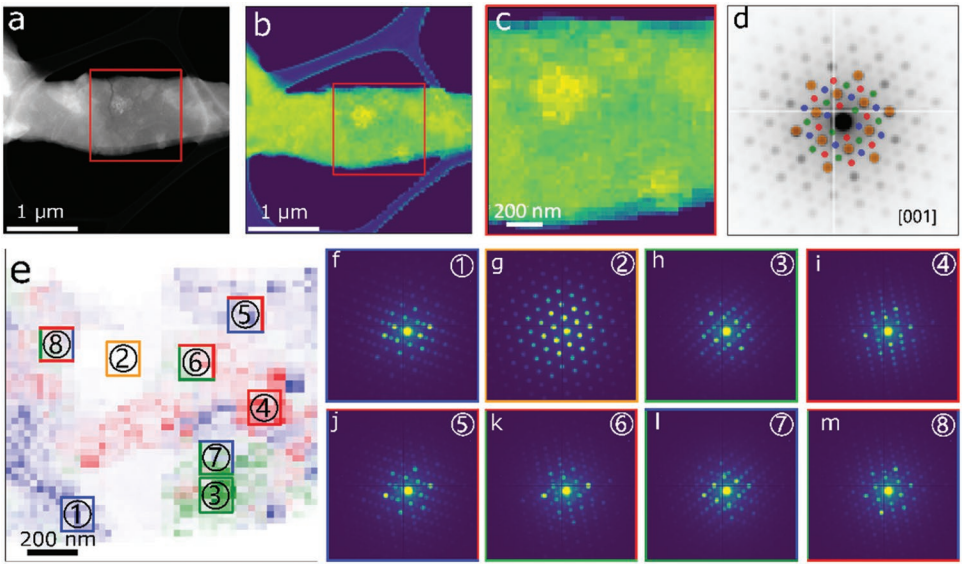

Figure 2. 4DSTEM results of a K-intercalated MoS_2 flake. a) is a HAADF-STEM image (1024 × 1024 pixels) of a K intercalated MoS_2 flake and b) is the virtual 4DSTEM summed intensity image of the same region (128 × 128 pixels, shown with a false colour temperature scale). The red square selects a single crystal area that is shown magnified in the virtual summed intensity image in c) (50×50 pixels). d) shows the summed electron diffraction data for the selected area shown in (c) where the superlattice reflections for different scattering orientations are highlighted by red, green, and blue virtual objective apertures and the MoS_2 host lattice reflections are marked by the orange virtual objective apertures. e) is the composite computed DF image showing the ordering in the three superlattice orientations (the spatial distribution of the MoS_2 host lattice reflections is shown in Figure S12a, Supporting Information). The color scale represents the different superlattice orientations (corresponding diffraction patterns shown in f, h, i). (f)–(m) are the average diffraction pattern calculated for the 8 selected regions of interest in (e) (each 5 × 5 pixels). g) illustrates just the host MoS_2 pattern (without K ordering). j–l) display mixtures of two different components. m) shows all three components superimposed within one pattern.

© 2023 The Authors. Advanced Functional Materials published by Wiley-VCH GmbH

16163028, 0, Downloaded from https://onlinelibrary.wiley.com/doi/10.1002/adfm.202214390 by Danish Technical Knowledge, Wiley Online Library on [14/06/2023]. See the Terms and Conditions (https://onlinelibrary.wiley.com/terms-and-conditions) on Wiley Online Library for rules of use; OA articles are governed by the applicable Creative Commons License

giving rise to these different $2a \times 4a$ superlattice spots are not identical as shown by the false coloured regions in Figure 2e. In fact, the 4D-STEM analysis reveals that the $2a \times 2a$ structure is formed by the presence of all three $2a \times 4a$ basis superlattices with different orientations, having uncorrelated spatial distributions in the basal plane. These $2a \times 4a$ superlattice domains have dimensions of 10s nm to 100s nm (the domains are shown separately in SI Figure S12a-d, Supporting Information). Single pixels composed of multiple colours represent where two or three basis superlattices overlap (see SI Figure S14c,d, Supporting Information for examples of individual pixel data). To illustrate the variety of electron diffraction patterns that can result from this nanoscale structural variability we simulate virtual SAED apertures (~100 nm diameter, 5×5 pixels) for eight representative regions (coloured squares in Figure 2e) and generate diffraction patterns for these regions as shown in Figure 2f-m (further examples in SI Figure S15, Supporting Information). All patterns can be simulated by combining the three $2a \times 4a$ superlattices and the pristine MoS_2 host with different weightings (SI Figure S10e-g, Supporting Information). Another example of the uncorrelated spatial distribution of superlattice domains in the host lattice is given in SI Figure S13 (Supporting Information). To our knowledge there is only one previous example where nanoscale superlattice domains have been identified in $NaMoS_2$, but this study used high-resolution TEM imaging so understanding of structural variations was limited by the challenge of image interpretation.[26] The 4D-STEM approach used here enables more robust nanoscale orientation mapping of larger areas and demonstrates the presence of lower symmetry nanoscale domains for the whole sample, which overlap in the [0001] direction. This new structural understanding suggests that historical SAED literature, proposing regular interpenetrating layers of ordered alkali metals, will likely need to be reanalysed with this in mind.

3. Structural and Compositional Changes during Deintercalation

To understand how the intercalated K_nMoS_2 flakes change during deintercalation we employ a combination of nanoscale elemental analysis (STEM-EDS maps) and electron diffraction (SAED) to study the materials' dynamic evolution when annealing at different temperatures in the TEM. This in situ approach avoids the risk of degradation due to accidental exposure of the intercalated flakes to air. It also allows consistent monitoring of changes within the same sample regions in real time, which is essential when the material displays such nanoscale heterogeneity. Our in situ studies employed fixed temperatures of 25, 150, 200, and 300 °C, a range which encompasses typical temperatures used in the fabrication of K-doped MoS_2 devices and their working conditions.[4] Figure 3g shows a schematic of the in situ TEM experimental setup, where K-doped MoS_2 flakes are dispersed on a resistive heating membrane and holes in the membrane allow analysis of fully suspended 2D flakes.

Figure 3a–d shows consecutive in situ SAED patterns acquired from a $K_{0.65}MoS_2$ crystal at hourly increments at a temperature of 300 °C, where changes in the spot positions and intensities are evidence of compositional and structural changes that occur during deintercalation. Splitting of the $11\bar{2}0$ spot in Figure 3a reveals both pristine and expanded intercalated basal plane regions are present in the starting material as discussed previously. The $11\bar{2}0$ spot shown in the inset demonstrates that at $t = 0$ the inner (expanded) peak, corresponding to the intercalated lattice, has a higher intensity than the peak for the pristine 2H-MoS_2. After 2 h there is a notable decrease in the intensity of the inner (intercalated) spot and of the superlattice, and after 3 h neither the inner spot nor the superlattice is visible (insets in Figure 3b–d and Figure 3e,f, also see Figure S16, Supporting Information). Electron diffraction alone could therefore be interpreted as demonstrating that the structure is fully deintercalated 2H phase MoS_2. However, our EDS measurements show that significant K content remains associated with the flake even when the 2H phase is restored.

This apparent ambiguity is resolved by our combined STEM-EDS+SAED measurements such as shown in **Figure 4**. Here the diffraction pattern obtained for the as-prepared intercalated flake is consistent with the $K_{0.75}MoS_2$ superlattice atomic model presented in Figure 1f and the expected composition before annealing ($n = 0.75$, see Figure S11, Supporting Information). On heating at 300 °C for 1 h the K content decreases to $n = 0.61$ ($K_{0.61}MoS_2$) and new superlattice spots emerge, representing a doubling of the lattice period along the $[1\bar{1}00]$ direction (example positions are marked by the blue triangles in Figure 4e, g and magnified in the inset). Note that these new superlattice positions cannot be formed by chains of Mo (as in the 1T′, 1T″ or 1T‴ polytypes)[44], suggesting the superstructure is due to a new type of $2a \times \sqrt{3}a$ ordering of alkali ions. We can propose a 4 atomic layer unit cell that reproduces the observed diffraction pattern (as shown in Figure 4i) and provides a reasonable match to the measured elemental composition ($K_{0.625}MoS_2$). However, given our 4D-STEM evidence of nanodomains, a more likely interpretation is the presence of both $2a \times \sqrt{3}a$ and $2a \times 4a$ superlattices within the ≈100 nm regions of the selected area aperture. A ratio of 1:3 for $(2a \times \sqrt{3}a)$:$(2a \times 4a)$ superstructures reproduces close to the experimental atomic composition ($K_{0.625}MoS_2$,). The inclusion of a small proportion of 2H host lattice with a lower K content enables a precise compositional match (although we cannot rule out that K may be adsorbed on the surfaces which could increase the measured K content).

It is interesting that, as the mean K/Mo ratio decreases from $n = 0.75$ to $n = 0.61$ (20.0 at% K to 16.9 at%) under heating (Figure 4c), the standard deviation in the measurements also decreases from 0.32 to 0.16, indicating that K distribution in the flake becomes more uniform. Importantly, we do not find evidence of preferential loss of K at the edges as suggested by some deintercalation models. Rather, annealing-induced deintercalation acts to homogenize the composition of the whole crystal as evident from comparing the quantitative compositional line-scans before and after heating (Figure 4c and Figure S20, Supporting Information). Although the interplanar distance is not a good estimate of the level of K content in the material (see SI section S6), cross sectional HAADF STEM imaging during deintercalation as shown in **Figure 5** (see Figures S23,S24, Supporting Information for processing) supports the homogenization of the material during annealing with the standard deviation of the interlayer spacing reducing

© 2023 The Authors. Advanced Functional Materials published by Wiley-VCH GmbH

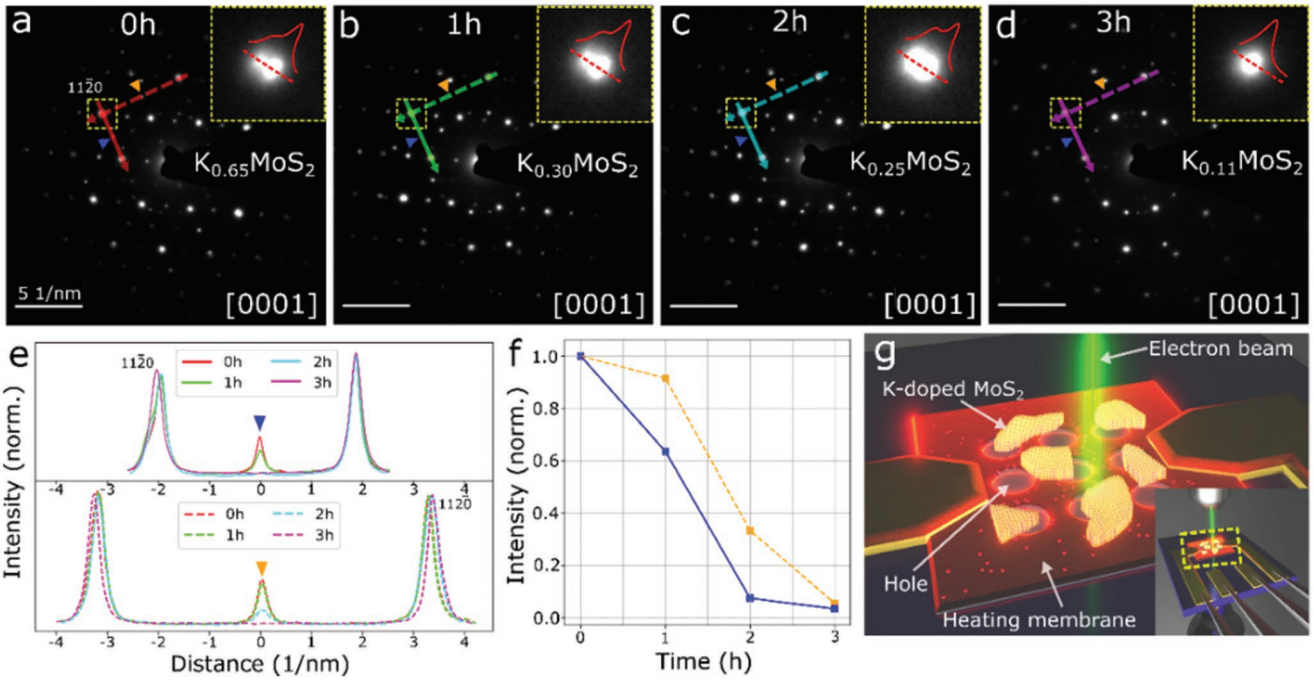

Figure 3. Phase transitions in K-doped MoS_2 observed by in situ SAED. Selected area electron diffraction patterns of a single K-doped MoS_2 flake captured a) before and b) after 1 h, c) 2 h, and d) 3 h heating at 300 °C, respectively. Insets in (a–d) show the splitting of the $11\bar{2}0$ diffraction spots, and how this evolves during heating. The relative peak intensities in the extracted $11\bar{2}0$ intensity profiles are further analysed in Figure S16 (Supporting Information). The solid and dashed arrows indicate the positions of the extracted intensity profiles shown in e). The orange and blue triangle markers indicate the positions of two reciprocal superlattice spots the intensity of which is shown in f). (e) Comparison of the intensity profiles from the in situ SAED patterns for two crystallographic directions (marked by the solid and dashed lines in (a–d)). f) Demonstration of the loss of superlattice spot intensity, measured from line profiles (e), as a function of heating time. g) Schematic illustration of the K-doped MoS_2 flakes on the resistive heating E-chip membrane.

from 0.1 to 0.05. Additionally, defects appearing to "heal", as shown in the insets of Figure 5a–d, which is encouraging for the potential regeneration of degraded MoS_2-based electrodes. This demonstration of synchronized elemental and structural changes at the micrometer scale, even in the presence of large heterogeneity at the nanoscale, gives confidence that the mean intercalated starting composition and knowledge of the rate of deintercalation can be used to quantitatively predict the compositional evolution behavior.

To achieve this aim, STEM-EDS analysis was performed for 5 separate flake agglomerates at each temperature (25, 150, 200 or 300 °C) for up to 3 h. To ensure accuracy and reproducibility, 1300–1700 individual pixel (spectra) measurements were performed for each flake (see Supporting Information section 5). To account for the initial variability in intercalated K concentration within the flakes before heating, we have normalized the atomic ratio of K/Mo to the specific flake's starting composition and use this as a metric for change in K concentration (Figure 4k). The K/Mo ratio of a specimen is unchanged (<1.5%) over 4 h at room temperature (Figure S21a, Supporting Information), in agreement with previous reports of successful long-term storage of intercalated 2D materials at room temperature under inert gas or vacuum conditions.[21] This control data also serves to exclude any possible electron beam induced deintercalation effects, as the room temperature specimen received the same electron fluence as the heated samples.

Fitting the n versus t plots in Figure 4k demonstrates an exponential decay in the K content during heating, which can be fitted to the following function:

$$N(t) = N_0\, e^{-kt} \tag{1}$$

where N(t) and N_0 represent the concentration at time t and time 0 respectively, k is the effective rate constant of K deintercalation in a MoS_2 crystal at a specific temperature and can be obtained via measuring the slope of each linear regression shown in Figure S21e (Supporting Information). This exponential relationship is indicative of first-order kinetics and fitting the data to the Arrhenius equation gives a linear relationship between the reaction rate constant, k, and inverse temperature, $1/T$, shown in Figure 4m:

$$\ln(k) = -2414.76 \times \frac{1}{T} + 3.03 \tag{2}$$

This empirical model allows prediction of the rates of K deintercalation in K-doped MoS_2 for a given temperature and heating time. Understanding this relationship is important for applications where sample preparation requires annealing of K_nMoS_2 or where the material is used at elevated temperatures. Although the results presented here are applicable to K_nMoS_2 in vacuum or inert gas environments, the approach could be extended to other intercalated or pillared nanomaterials and

© 2023 The Authors. Advanced Functional Materials published by Wiley-VCH GmbH

16163028, 0, Downloaded from https://onlinelibrary.wiley.com/doi/10.1002/adfm.202214390 by Danish Technical Knowledge, Wiley Online Library on [14/06/2023]. See the Terms and Conditions (https://onlinelibrary.wiley.com/terms-and-conditions) on Wiley Online Library for rules of use; OA articles are governed by the applicable Creative Commons License

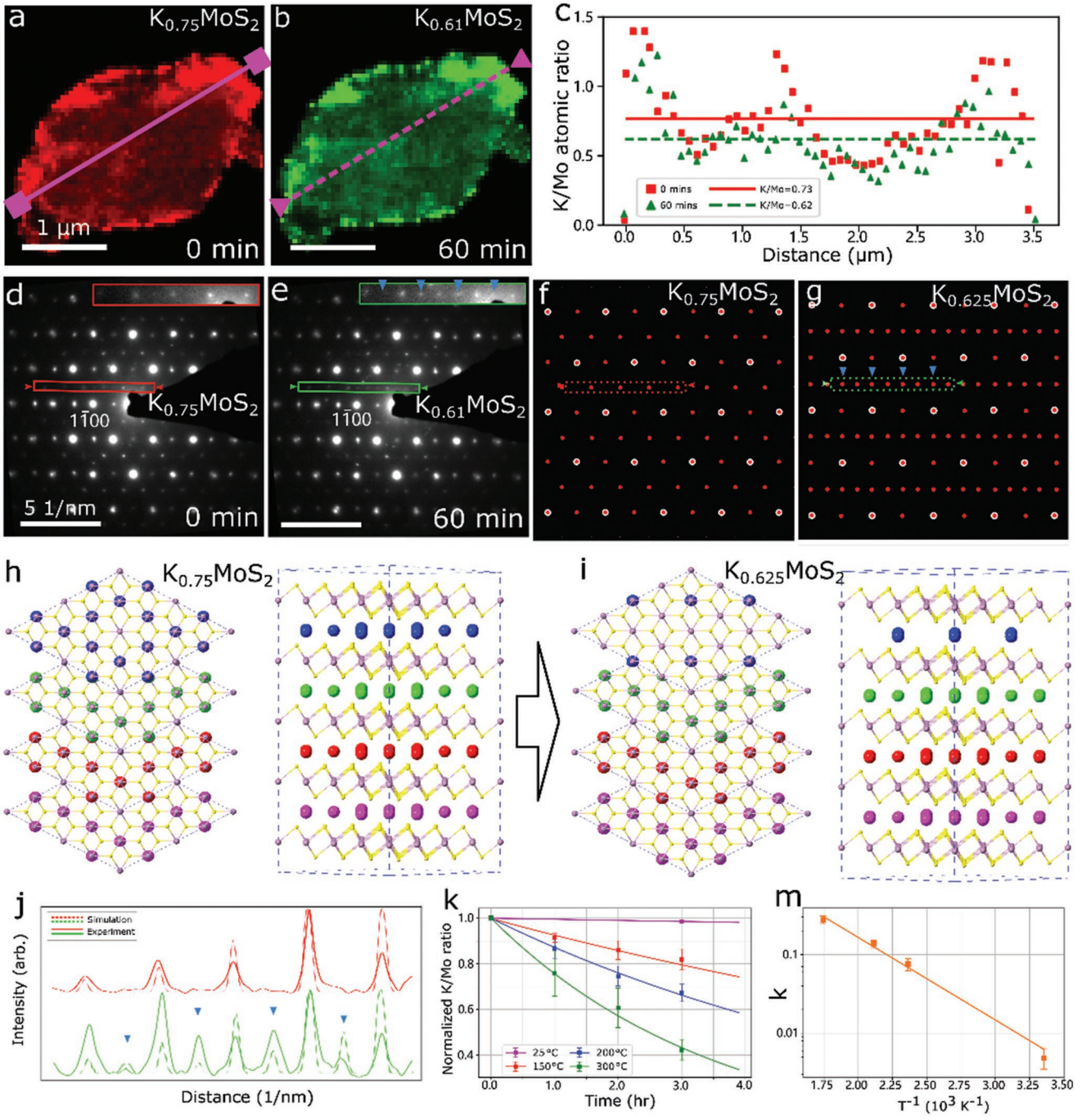

Figure 4. STEM EDS mapping and TEM characterisation of the K deintercalation process. a, b) K/Mo ratio STEM-EDS elemental maps of a same flake acquired before (a) and after 60 min heating at 300 °C b). Mean K concentrations measured for the entire flake are indicated top right. c) Comparison of the atomic ratio of K/Mo along magenta lines shown in (a) and (b). Mean values are plotted as the solid red line for before annealing and the dashed green line after annealing. d, e) Selected area diffraction patterns of the flakes shown in (a, b) respectively. The insets highlight the location of the extra reciprocal superlattice spots that appear in (e), indicated by blue triangles. f, g) Simulated diffraction patterns obtained for atomic models with compositions of $K_{0.75}MoS_2$ and $K_{0.625}MoS_2$ respectively (crystal structures are shown in h, i) with further details in Figure S11 and S17, Supporting Information). j) Comparison of normalised experimental and simulated intensity across (d, e) electron diffraction and (f, g) the simulated patterns. The discrepancy between amplitude of measured and simulated may be due to slightly tilting of the specimen and the difference of the thickness. k) Plot of the exponential decay for the normalised K/Mo ratio detected from the K-doped MoS_2 flakes at four different temperatures (25, 150, 200, and 300 °C). m) Arrhenius plot of the rate constant for K deintercalation against inverse temperature on a semi-ln scale.

© 2023 The Authors. Advanced Functional Materials published by Wiley-VCH GmbH

16163028, 0, Downloaded from https://onlinelibrary.wiley.com/doi/10.1002/adfm.202214390 by Danish Technical Knowledge, Wiley Online Library on [14/06/2023]. See the Terms and Conditions (https://onlinelibrary.wiley.com/terms-and-conditions) on Wiley Online Library for rules of use; OA articles are governed by the applicable Creative Commons License

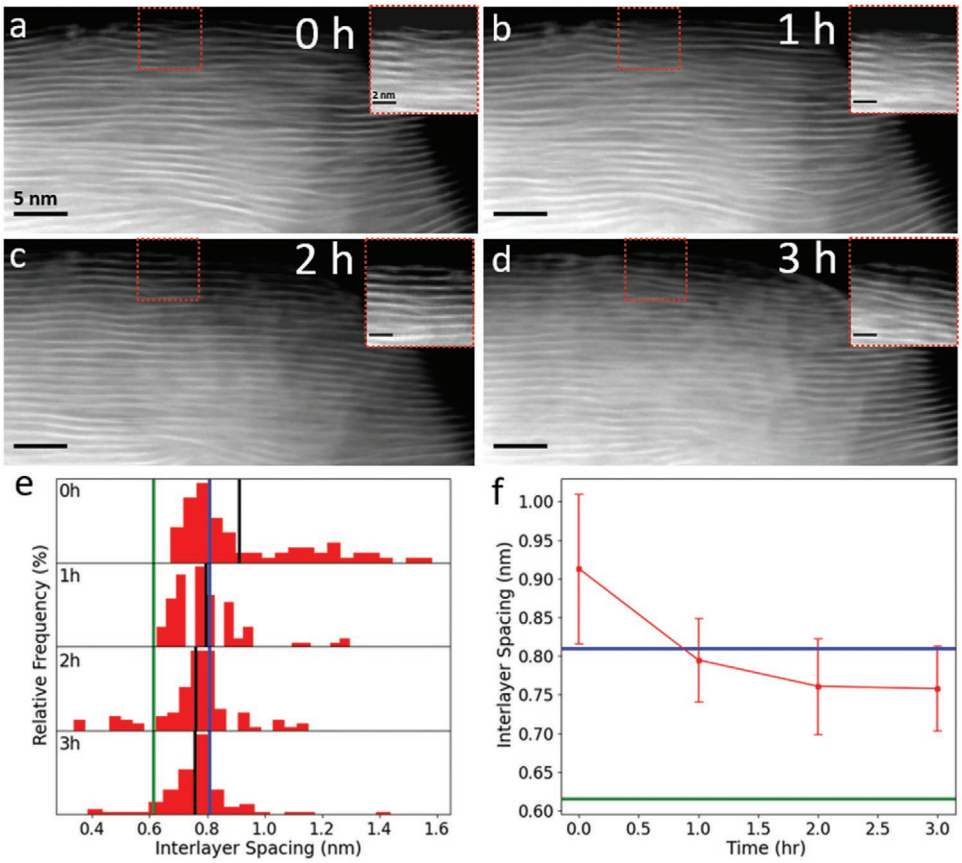

Figure 5. In situ high-resolution STEM imaging of interlayer structures for K-doped MoS_2. a – d) High-resolution HAADF STEM images from the edge of single flake over 3 h of heating at 200 °C. Shaded areas represent the positions of large interlayer spacings suggested to consist of nanoscale K domains. The insets show enlarged views illustrating the healing of the defective atomic layer structure. e) Measured distribution of interlayer distances as a function of annealing. Black, green, and blue lines illustrate the mean interlayer spacing in the sample, pristine MoS_2,[11,16] and interlayer spacing of K intercalated MoS_2,[16,51] respectively. f) Plot of the variation of the mean interlayer distance during annealing, with the standard deviation in measurements shown by the error bars.

more oxidative conditions could be investigated using an in situ gas cell and similar methodologies.

4. Conclusion

In summary, the nanoscale structural and compositional variation of intercalated K_nMoS_2 flakes was investigated using a combined 4D-STEM and in situ elemental analysis approach, which we propose is widely applicable to 2D materials that undergo complex, dynamic structural and chemical changes. The large variations in composition, polytype and interlayer spacing seen here at the nanoscale suggest that the structure of thin K intercalated MoS_2 flakes is poorly described by any average unit cell, even where this gives a good match to the mean experimental composition and diffraction data (illustrated in Figure S25, Supporting Information). The intercalated material was predominantly found to consist of $2a \times 4a$ superstructure domains with widths of 10–100 nm, coexisting with the host 2H lattice. We also identify the $2a \times \sqrt{3}a$ superstructure in this system for the first time. During deintercalation we observe the potential for different local superstructure formations to emerge, and that these can have $2a \times 2a$, $2a \times \sqrt{3}a$, and $2a \times 4a$ type ordering of the alkali ions. However, overall deintercalation acts to decrease the variance of the local elemental composition and interlayer spacings, suggesting a route to synthesis of more homogeneous intercalated materials. In situ measurements of the deintercalation process revealed this is determined by first-order kinetics and provides an empirical formula for predicting the deintercalation rate for the material under specific operating conditions.

5. Experimental Section

K-doped MoS_2 powder was prepared via the liquid ammonia method where the pristine 2H-MoS_2 powder (Aldrich 99%) and K metal (Aldrich 95%) were sealed in a quartz reactor tube in the inert atmosphere of a glovebox (oxygen < 0.5 ppm, moisture < 0.5 ppm). The tube was then evacuated to ≈10^{-5} mbar and placed in a bath of dry ice/ethanol to keep it at a low temperature (≈-78 °C). The reactor was filled with high-purity ammonia gas (CK Gas 99.98%), which liquefies and dissolves the K metal to form a deep blue solution of K in liquid ammonia. The residual volume left by liquification of the ammonia gas was filled by high-purity Ar gas to prevent the sample from oxidizing. The reactor was kept in dry

© 2023 The Authors. Advanced Functional Materials published by Wiley-VCH GmbH

16163028, 0, Downloaded from https://onlinelibrary.wiley.com/doi/10.1002/adfm.202214390 by Danish Technical Knowledge, Wiley Online Library on [14/06/2023]. See the Terms and Conditions (https://onlinelibrary.wiley.com/terms-and-conditions) on Wiley Online Library for rules of use; OA articles are governed by the applicable Creative Commons License

ice/ethanol bath for 24 h for the required degree of intercalation. Finally, ammonia was pumped out of the reactor and K-doped crystals were taken out while sealed in a closed container, and stored in the glovebox.

For in situ S/TEM imaging the as-prepared powder was dry-cast on the holey carbon coated ceramic resistive heating membrane of a Thermal E-chip from Protochips Inc. (Raleigh, NC) and the E-chip was mounted onto a double-tilt Protochips Aduro sample holder in the glovebox. The holder was then transferred to the TEM sealed in an Ar filled box and loaded quickly into the instrument to minimize exposure to air (≈a few seconds). SAED was performed in an FEI Tecnai G2 20 TEM operated at 200 kV with a 0.21±0.1 µm SAED aperture and an FEI Tecnai TF30 FEG-AEM operated at 300 kV with a 0.87±0.1 µm SAED aperture. High angle annular dark field (HAADF) STEM imaging was performed in an FEI Titan G2 80–200 "ChemiSTEM" operated at 200 kV with a 21 mrad probe convergence angle, an aberration corrected probe and a HAADF inner angle of 64 mrad. STEM-EDS data was acquired using the Titan's Super-X EDS detector system (quad chip with a total collection solid angle ≈0.7 srad) and on the TF30 TEM using a SDD X-ray detector from Oxford instrument. Hyperspy was used to process all STEM-EDS data.[45] To gain accurate compositional analysis for individual flakes from the STEM-EDS spectrum images, we employed binary masking, local averaging and standardless Cliff Lorimer k-factor quantification (see Figure S18, Supporting Information for further details). HAADF simulations were performed with the QSTEM package[46] using the above experimental parameters with Cs = 0 mm and Cc = 1 mm. Electron diffraction patterns were simulated using the multislice method[47] implemented with the code developed by Kirkland.[48]

The 4DSTEM datasets were acquired using the MerlinEM direct electron detector placed at the bottom of the Talos TEM. Every 4DSTEM dataset consists of 16384 single diffraction patterns recorded from a region (128 × 128 pixels). The semi-convergence angle (1.52 mrad) of the electron probe employed in 4DSTEM acquisition, and the camera length of 205 mm was chosen in order to detect clearly separated diffracted disks. To optimize the signal-to-noise ratio without introducing significant beam damages to the sample, the probe current was ≈56 pA and the dwell time 50 ms resulting in a total dose of 2.3×10^5 e^-nm^{-2} which is in a safe range (determined as $< 2.6 \times 10^5 e^-nm^{-2}$ as shown in the supporting information) to prevent the sample being degraded by the electron beam. The evaluation of the 4DSTEM datasets was performed by python packages: Hyperspy,[49] py4DSTEM,[50] and pyxem.[51] More detail on the 4DSTEM technique is provided in Supporting Information section S3.

Supporting Information

Supporting Information is available from the Wiley Online Library or from the author.

Acknowledgements

The authors gratefully acknowledge support from the Engineering and Physical Sciences Research Council (EPSRC) Graphene NOWNANO Centre for Doctoral Training for a provision of a PhD studentship, EPSRC PhD plus award and EPSRC Doctoral Prize Fellowship. The authors acknowledge funding from EPSRC (EP/P009050/1), Lloyd's Register Foundation and from the European Research Council under the Horizon 2020 program for the ERC Starter Grant EvoluTEM (715502). This work was supported by the Henry Royce Institute for Advanced Materials, funded through EPSRC grants EP/R00661X/1, EP/S019367/1, EP/P025021/1, and EP/P025498/1.

Conflict of Interest

The authors declare no conflict of interest.

Data Availability Statement

The data that support the findings of this study are available from the corresponding author upon reasonable request.

Keywords

alkali metal intercalation, EDS spectrum imaging, energy dispersive X-ray spectroscopy, first-order kinetics, in situ S/TEM, KMoS2, SAED

Received: December 9, 2022
Revised: March 20, 2023
Published online:

[1] L. Zhao, R. Zhang, C. Deng, Y. Peng, T. Jiang, *Nanomaterials* **2019**, *9*, 1096.
[2] J. L. Hart, K. Hantanasirisakul, A. C. Lang, B. Anasori, D. Pinto, Y. Pivak, J. T. van Omme, S. J. May, Y. Gogotsi, M. L. Taheri, *Nat. Commun.* **2019**, *10*, 522.
[3] R. Friend, A. Yoffe, *Adv. Phys.* **1987**, *36*, 1.
[4] F. Zeng, X. Xi, H. Cao, Y. Pei, H. J. Heeres, R. Palkovits, *Appl. Catal., B* **2019**, *246*, 232.
[5] O. Salihoglu, H. B. Uzlu, O. Yakar, S. Aas, O. Balci, N. Kakenov, S. Balci, S. Olcum, S. Süzer, C. Kocabas, *Nano Lett.* **2018**, *18*, 4541.
[6] K. Hantanasirisakul, M. Alhabeb, A. Lipatov, K. Maleski, B. Anasori, P. Salles, C. Ieosakulrat, P. Pakawatpanurut, A. Sinitskii, S. J. May, Y. Gogotsi, *Chem. Mater.* **2019**, *31*, 2941.
[7] R. Kappera, D. Voiry, S. E. Yalcin, B. Branch, G. Gupta, A. D. Mohite, M. Chhowalla, *Nat. Mater.* **2014**, *13*, 1128.
[8] R. Nishitani, Y. Uno, H. Suematsu, *Phys. Rev. B* **1983**, *27*, 6572.
[9] F. Xiong, H. Wang, X. Liu, J. Sun, M. Brongersma, E. Pop, Y. Cui, *Nano Lett.* **2015**, *15*, 6777.
[10] K. Sun, H. Guo, F. Jiao, Y. Chai, Y. Li, B. Liu, S. Mintova, C. Liu, *Appl. Catal., B* **2021**, *286*, 119907.
[11] R. Zhang, I. L. Tsai, J. Chapman, E. Khestanova, J. Waters, I. V. Grigorieva, *Nano Lett.* **2016**, *16*, 629.
[12] J. Peng, Y. Liu, X. Luo, J. Wu, Y. Lin, Y. Guo, J. Zhao, X. Wu, C. Wu, Y. Xie, *Adv. Mater.* **2019**, *31*, 1900568.
[13] X. Du, J. Huang, X. Guo, X. Lin, J.-Q. Huang, H. Tan, Y. Zhu, B. Zhang, *Chem. Mater.* **2019**, *31*, 8801.
[14] X. Ren, Q. Zhao, W. D. McCulloch, Y. Wu, *Nano Res.* **2017**, *10*, 1313.
[15] R. Schöllhorn, in *Progress in Intercalation Research*, (Eds: W. Müller-Warmuth, R. Schöllhorn), Springer, Dordrecht, Netherlands **1994**, 1.
[16] R. Zhang, I.-L. Tsai, J. Chapman, E. Khestanova, J. Waters, I. V. Grigorieva, *Nano Lett.* **2016**, *16*, 629.
[17] Y. Fang, X. Hu, W. Zhao, J. Pan, D. Wang, K. Bu, Y. Mao, S. Chu, P. Liu, T. Zhai, F. Huang, *J. Am. Chem. Soc.* **2019**, *141*, 790.
[18] B. Pal, A. Singh, S. G. , P. Mahale, A. Kumar, S. Thirupathaiah, H. Sezen, M. Amati, L. Gregoratti, U. V. Waghmare, D. D. Sarma, *Phys. Rev. B* **2017**, *96*, 195426.
[19] D. Voiry, M. Salehi, R. Silva, T. Fujita, M. Chen, T. Asefa, V. B. Shenoy, G. Eda, M. Chhowalla, *Nano Lett.* **2013**, *13*, 6222.
[20] M. A. Santa-Ana, V. Sanchez, G. Gonzalez, *Electrochim. Acta* **1995**, *40*, 1773.
[21] R. Somoano, V. Hadek, A. Rembaum, *J. Chem. Phys.* **1973**, *58*, 697.
[22] M. Acerce, D. Voiry, M. Chhowalla, *Nat. Nanotechnol.* **2015**, *10*, 313.
[23] K. Xie, K. Yuan, X. Li, W. Lu, C. Shen, C. Liang, R. Vajtai, P. Ajayan, B. Wei, *Small* **2017**, *13*, 1701471.
[24] C. Ghosh, M. K. Singh, S. Parida, M. T. Janish, A. Dobley, A. M. Dongare, C. B. Carter, *Sci. Rep.* **2021**, *11*, 9014.
[25] L. Wang, Z. Xu, W. Wang, X. Bai, *J. Am. Chem. Soc.* **2014**, *136*, 6693.

© 2023 The Authors. Advanced Functional Materials published by Wiley-VCH GmbH

16163028, 0, Downloaded from https://onlinelibrary.wiley.com/doi/10.1002/adfm.202214390 by Danish Technical Knowledge, Wiley Online Library on [14/06/2023]. See the Terms and Conditions (https://onlinelibrary.wiley.com/terms-and-conditions) on Wiley Online Library for rules of use; OA articles are governed by the applicable Creative Commons License

[26] P. Gao, L. Wang, Y. Zhang, Y. Huang, K. Liu, *ACS Nano* **2015**, *9*, 11296.
[27] Q. Huang, X. Li, M. Sun, L. Zhang, C. Song, L. Zhu, P. Chen, Z. Xu, W. Wang, X. Bai, *Adv. Mater. Interfaces* **2017**, *4*, 1700171.
[28] M. T. Janish, C. B. Carter, *Scr. Mater.* **2015**, *107*, 22.
[29] W. Rudorff, *Chimia* **1965**, *19*, 489.
[30] R. Catterall, N. Mott, *Adv. Phys.* **1969**, *18*, 665.
[31] M. H. Cohen, J. C. Thompson, *Adv. Phys.* **1968**, *17*, 857.
[32] J. Heising, M. G. Kanatzidis, *J. Am. Chem. Soc.* **1999**, *121*, 638.
[33] K. Chrissafis, M. Zamani, K. Kambas, J. Stoemenos, N. Economou, I. Samaras, C. Julien, *Mater. Sci. Eng., B* **1989**, *3*, 145.
[34] A. Zak, Y. Feldman, V. Lyakhovitskaya, G. Leitus, R. Popovitz-Biro, E. Wachtel, H. Cohen, S. Reich, R. Tenne, *J. Am. Chem. Soc.* **2002**, *124*, 4747.
[35] A. Andersen, S. M. Kathmann, M. A. Lilga, K. O. Albrecht, R. T. Hallen, D. Mei, *J. Phys. Chem. C* **2012**, *116*, 1826.
[36] Q. Huang, L. Wang, Z. Xu, W. Wang, X. Bai, *Sci. China: Chem.* **2018**, *61*, 222.
[37] M. Watanabe, in *Scanning Transmission Electron Microscopy: Imaging and Analysis* (Eds: S. J. Pennycook, P. D. Nellist), Springer, NY, USA **2011**, 291.
[38] M. Watanbe, A. Yasuhara, E. Okunishi, *JEOL. News* **2010**, *45*, 8.
[39] V. J. Keast, D. B. Williams, *Acta Mater.* **1999**, *47*, 3999.
[40] M. Watanabe, D. W. Ackland, A. Burrows, C. J. Kiely, D. B. Williams, O. L. Krivanek, N. Dellby, M. F. Murfitt, Z. Szilagyi, *Microsc. Microanal.* **2006**, *12*, 515.
[41] C. Ophus, *Microsc. Microanal.* **2019**, *25*, 563.
[42] P. Phillips, M. Brandes, M. Mills, M. De Graef, *Ultramicroscopy* **2011**, *111*, 1483.
[43] L. A. Jácome, G. Eggeler, A. Dlouhý, *Ultramicroscopy* **2012**, *122*, 48.
[44] C. Habenicht, A. Lubk, R. Schuster, M. Knupfer, B. Büchner, *Phys. Rev. B* **2020**, *101*, 155429.
[45] F. de la Peña, E. Prestat, V. Tonaas Fauske, P. Burdet, P. Jokubauskas, M. Nord, T. Ostasevicius, K. E. MacArthur, M. Sarahan, D. N. Johnstone, *Zenodo* **2019**, https://doi.org/10.5281/zenodo.592838.
[46] C. T. Koch, *Determination of core structure periodicity and point defect density along dislocations*, *Ph.D. Thesis*, Arizona State University, Tempe, Arizona **2002**.
[47] J. M. Cowley, A. F. Moodie, *Acta Crystallogr.* **1957**, *10*, 609.
[48] E. J. Kirkland, *Advanced computing in electron microscopy*, Springer, Berlin, Germany **1998**.
[49] B. H. Savitzky, S. E. Zeltmann, L. A. Hughes, H. G. Brown, S. Zhao, P. M. Pelz, T. C. Pekin, E. S. Barnard, J. Donohue, L. Rangel DaCosta, E. Kennedy, Y. Xie, M. T. Janish, M. M. Schneider, P. Herring, C. Gopal, A. Anapolsky, R. Dhall, K. C. Bustillo, P. Ercius, M. C. Scott, J. Ciston, A. M. Minor, C. Ophus, *Microsc. Microanal.* **2021**, *27*, 712.
[50] D. N. Johnstone, P. Crout, J. Laulainen, S. Høgås, B. Martineau, T. Bergh, S. Smeets, S. Collins, J. Morzy, H. Ånes, *Zenodo* **2019**, https://doi.org/10.5281/zenodo.2649351.
[51] J. Wei, P. He, J. Wu, N. Chen, T. Xu, E. Shi, C. Pan, H. Jia, A. Wang, *Fuel* **2022**, *311*, 122615.

© 2023 The Authors. Advanced Functional Materials published by Wiley-VCH GmbH

16163028, 0, Downloaded from https://onlinelibrary.wiley.com/doi/10.1002/adfm.202214390 by Danish Technical Knowledge, Wiley Online Library on [14/06/2023]. See the Terms and Conditions (https://onlinelibrary.wiley.com/terms-and-conditions) on Wiley Online Library for rules of use; OA articles are governed by the applicable Creative Commons License